Excimer laser ablation of graphite: The enhancement of carbon dimer formation

C. Ursu, P. Nica, C. Focsa

Excimer laser ablation of graphite: the enhancement of carbon dimer formation

C. Ursu[1], P. Nica[2,*], and C. Focsa[3]
[1] *"Petru Poni" Institute of Macromolecular Chemistry, 41 A Gr. Ghica Voda Alley, Iasi 700487, Romania*
[2] *Department of Physics, "Gheorghe Asachi" Technical University, Iasi, 700050, Romania*
[3] *Univ. Lille, CNRS, UMR 8523, PhLAM – Physique des Lasers, Atomes et Molécules, CERLA – Centre d'Etudes et de Recherches Lasers et Applications, F-59000 Lille, France*

Abstract:
Carbon plasmas produced by laser ablation can have important applications in the synthesis of nanostructured materials of high current interest (nanotubes, nanowires, graphene) or the deposition of diamond-like thin films. Understanding the fundamental aspects of such transient plasmas in various experimental configurations is useful for optimization of these synthesis/deposition processes. We report here a comprehensive study on the dynamics of an excimer laser produced carbon plasma, including fast photography, space- and time-resolved optical emission spectroscopy, Faraday cup ion current measurements, ablated crater depth profiling. A peculiar V-like shape of the emitting plume is evidenced and explained by the interaction of three plasma structures originating in distinct irradiance areas of the laser spot on the target. The interaction of these structures is also thought to favor an enhanced carbon dimer production, mainly through three-body recombination, at distances significantly higher than previously reported in the literature, which can find technological applications for the efficient deposition of high quality carbon-based nanostructures.

Keywords: excimer laser ablation, carbon plasma, carbon dimer, ablation crater, transient plasma dynamics

1. Introduction

Investigation of carbon laser-produced plasma (LPP) dynamics and composition is essential for the optimized production of nanostructured materials, including carbon nanotubes, nanowires, graphene, etc. [1–3], so as to enhance their properties and to gain control on the deposition process. The kinetic properties of LPP species and their ionization stage, which may be affected by ambient gas pressure, were found to strongly affect the deposited film quality [4]. For example, using a neutral background gas was found to influence the stoichiometric and structural properties of the pulsed laser deposited (PLD) diamond like carbon (DLC) films: an enriched content of sp^3 bonds, specific to DLC, were obtained for pressures below 200 mTorr, while for higher pressures the sp^2 bonds characterizing the amorphous carbon become dominant [5,6].

Regarding to the composition, among various species contained in transient LPP, carbon dimers C_2 play a significant role in clusters and nanoparticles production, and fundamental studies were performed to understand the physical mechanisms behind their formation. According with [7], for carbon LPP expansion in vacuum, the presence of C_2 is evidenced at short distances from the target and early expansion times. The background gas extends the region of C_2 formation, which is attributed to a three-body recombination mechanism, while some previous works [8–10] suggested the C_2 molecules are ejected directly from the target. The addition of a working gas leads to the formations of C_2 in larger regions and the identified spectral features proved that C_2 emission becomes more intense, but confined to closer areas, when using nitrogen as background gas instead of helium [11].

Several works also focused on the improvement of C_2 production in PLD by different methods. For example, colliding plasmas [12,13] determine the formation of a hot stagnation region which is rich in carbon dimers [14,15]. Investigations of plasma produced by dual-wavelength (1064/532 nm) double-pulse laser ablation revealed the influence of the delay between pulses on the C_2 molecules emission

* Author for correspondence: email: pnica@tuiasi.ro

duration [16]. In a non-uniform magnetic field, radial and axial plasma confinement [17] or ablation plume splitting [18] were evidenced, thus suggesting the possibility of influencing the fraction of component species, and furthermore the formation of C_2 molecules.

Various techniques have been used to follow temporally and spatially the dynamics of carbon dimers in LPPs. Optical emission spectroscopy (OES) is the most frequent choice, where the well-known $d^3\Pi_g \rightarrow a^3\Pi_g$ Swan band of the neutral C_2 molecule [5,19] is monitored (usually with its vibrational structure). The method has the advantage to be non-intrusive and to be able to provide space- and time-resolved information on the excited species that are well adapted to the transient features of LPP, but it is limited at several microseconds by the plasma emission lifetime. Laser-induced fluorescence (LIF) imaging spectroscopy [10] was used for a longer time scale and gave a scenario for the evolution in ambient He of carbon clusters. Complementary, fast-gated imaging of the plumes recorded with an intensified CCD (ICCD) camera provides a global picture of plasma evolution, while electrical methods using Langmuir probe [20–22], Faraday cup (FC) and electrostatic ion energy analyzer [4,23] are used to study the charge and energy of carbon ions generated by laser ablation.

Despite the large number of works focused on the characterization of carbon LPP and of grown thin films, there are some peculiar features that are not fully understood, important both from fundamental physical mechanism perspective and for possible application in carbon nanostructures synthesis. In a previous paper [24], we briefly reported preliminary data on a V-shape plasma plume expansion for a particular focusing of the KrF ablation laser beam. Measurements of crater profile showed possible correlations with the plasma plume shape, while OES revealed the presence of C_2 molecules in the plasma "arms", but not near the substrate placed at 50 mm in front of the graphite target. When correlating with the ion signal recorded on axial direction using an electrostatic energy analyzer [25] in various focusing conditions, and interpreted through the shifted Maxwell-Boltzmann distribution function [26–29] an expected increase of global plasma temperature with laser fluence resulted. However, the centre-of-mass velocity behaved differently, a minimum being recorded at an intermediate fluence value of the considered range (from 1.06 J/cm^2 to 1.94 J/cm^2), that corresponds to a threshold value at which the V-shape structure appears [24,25].

Some particularities of excimer lasers, such as high beam divergence (dependent on beam axis) or high M^2 factors sometimes make challenging potential industrial applications or laboratory researches. Mitigation of these inconveniences can employ beam homogenizers or variable reflectivity mirrors as output coupler to remove ripples and secondary lobes of the beam energy profile [30], in order to fully exploit the benefit of using the high pulse energy of excimer lasers in the UV range. In our experiments, no supplementary optics was used to reshape the KrF laser energy distribution in the ablation spot, and therefore possible connections with the V-like plasma are further considered.

In the present paper, detailed investigations on carbon LPP dynamics are performed using ICCD imaging, crater profile measurements, OES and FC ion analyzer. Electrical measurements performed using an FC detector placed in various angular positions with respect to the short and the long axes of the laser beam are correlated with the results obtained by ICCD fast imaging and time- and space-resolved OES. Plasma parameters as expansion velocities, its ion species, and temperature are calculated as function of the delay after the laser pulse and laser fluence. This comprehensive study allows us to propose a possible scenario for the origin of the observed peculiar plasma shape and to ascertain some hypotheses on the carbon dimer formation.

2. Experimental details

Carbon plasma has been produced by ablation of a high purity (99.99%) pyrolytic graphite disc (1 mm thickness) using a KrF excimer laser (248 nm, 20 ns, 5 Hz). The experiments were performed in vacuum (10^{-6} mbar) or in Ar background gas (~$5\cdot10^{-2}$ mbar). The laser beam was directed onto the target surface at 45° incidence angle and focused through a spherical lens (L1) of 500 mm focal length (see Fig. 1a). The distance between the L1 lens and the target surface was varied in the 41-46 cm range and will be denoted as *LP* in the following. The pulse energy was maintained constant during all these measurements at 264 mJ. At the laser exit, the energy beam profile was typical for excimer lasers: top-hat on the long (*X*)

axis, and approximately Gaussian on the short (*Y*) axis (see Fig. 1b), while in the front of the focusing lens (L1, at 1 m away from laser exit), it slightly changes due to the beam divergence, as given in Fig. 1c. The laser fluence was varied in a low regime, below 3 J/cm^2, by changing the distance between the focusing lens and the target surface. Using the spot area on the target, we estimated values between 2.1 J/cm^2 for *LP* = 46 cm and 1.2 J/cm^2 for *LP* = 41 cm.

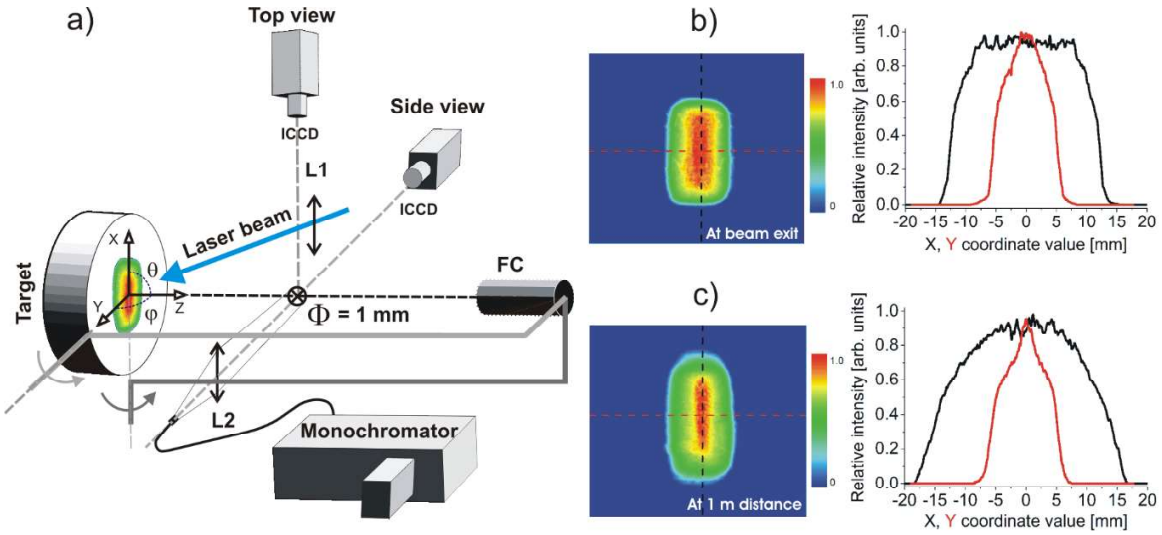

Fig. 1. Experimental setup for optical (OES and ICCD fast imaging) and electrical (Faraday cup) measurements of expanding plasma (a). Contour plot of beam energy distribution at excimer laser exit with the corresponding long-axis (*X*, black curve) and short-axis (*Y*, red curve) profiles (b), and similar plots in front of the focusing lens L1, at 1 m distance from the laser exit (c).

The global plasma emission at different delays with respect to the laser pulse was recorded by ICCD fast imaging (Andor iStar DH740-18U-03 camera) both in top and side views. Each image corresponds to a single laser pulse and 50 ns gate time. The space-resolved OES was performed by focusing emission from 1 mm diameter plasma regions with a 50 mm focal length spherical lens (L2, Fig. 1a) onto the 200 µm core diameter of an optical fiber connected to the entrance of a monochromator (Shamrock SR-303I-A, 33 cm focal length, 600 lines/mm grating, 0.3 nm spectral resolution). A mechanical translation system allowed spectra recording at various positions along the *X* and *Z* axes.

For ion current measurements, a Faraday cup (FC) was placed at a distance of 14 cm from the target surface, initially on the *Z*-axis of the ablation plume, *i.e.* normal to the target. Using a mechanical system, angular (θ,φ) rotations around the *X* and *Y* axes were possible, preserving the 14 cm FC distance to the impact point (see Fig. 1a). An aperture of 5 mm diameter was used at the entrance of the FC, to narrow the ion collecting area and to achieve a better spatial resolution. A voltage of -30 V applied on FC was determined to be sufficient for repelling the plasma electrons, thus avoiding their interference with the recorded ion saturation current. In order to avoid artifacts in the electrical signal, batteries were used for passively biasing the collector. The electrical signals were recorded by using the 50 Ω input impedance of a 2 GHz oscilloscope (LeCroy), externally triggered by a fast photodiode (2 ns rise time). Each recorded time-of-flight (TOF) signal was obtained as an average of ten laser shots directed onto fresh surfaces of the target, which was placed on an automated carousel control system.

3. Results and discussions

3.1. ICCD images and corresponding crater profiles

The global shape of the plasma expansion in vacuum was first recorded for various laser beam focusing (*LP*) conditions. In Fig. 2a we present typical side-view images (50 ns ICCD gate width) for *LP*

between 41 cm and 46 cm and for a constant delay of 2 μs from the laser pulse. A gradual change can be inferred, from a usual shape at lower fluence, which agrees with the top-hat energy distribution of the laser beam, to an unusual V-like plasma shape at increased focusing, having an angle between the radiating arms of about 30°. We note that the total plasma emissivity was observed to increase with the laser fluence, although the images from Fig. 2a were rescaled with respect to the maximum recorded intensity, in order to better distinguish the plasma shape. The ICCD images recorded at different delays for *LP*=46 cm (Fig. 2b) show that the V-shape plasma structure can be observed after the initial stages of expansion, having the origin in two "seeds" of plasma separated by ~10 mm in a plane parallel to the target, which are formed after ~150 ns from the laser pulse. Along the normal direction to the target surface, there are initially fast ejected particles, leaving behind them two radiating lateral arms. As can be observed from the ICCD images, the light emission from this central plasma structure is of lower intensity compared to the lateral arms. The existence of two types of particles (plasma structures) which are formed during the expansion process is well-known in the literature [31–34]. They consist in a fast (hot) part containing highly charged particles ejected at early moments, accelerated through the electric field generated by the charge separation, and a slow (cold) tail of low average charge state particles ejected through thermal processes [35–37].

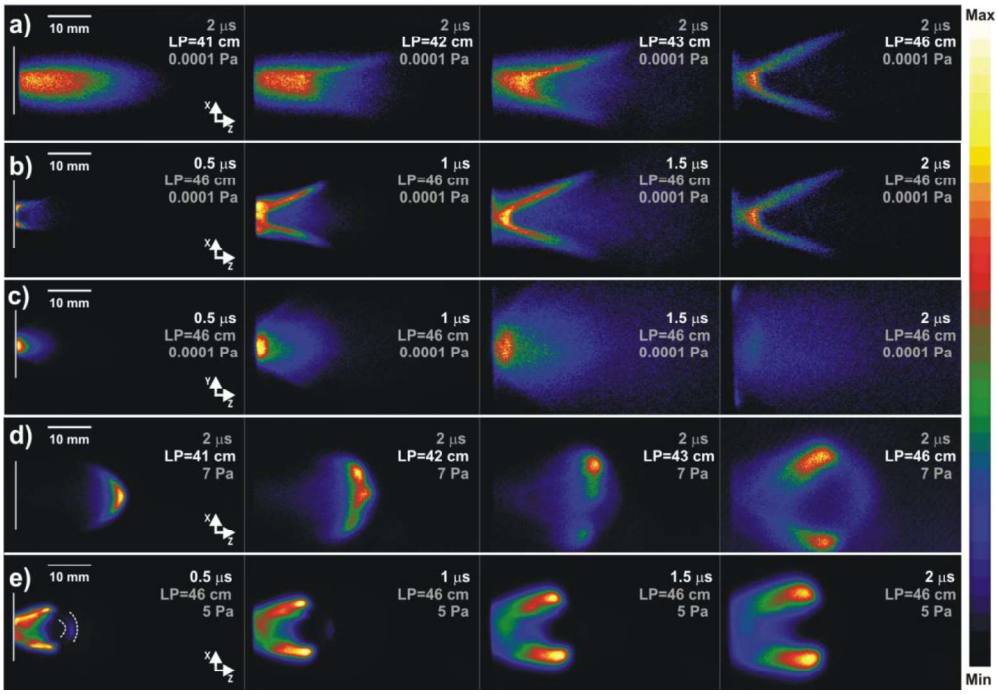

Fig. 2. Spectrally integrated ICCD images of carbon laser-produced plasma: at 2 μs after the laser pulse, for various focusing conditions (a), and from the side (b) and top (c) perspective at various stages of expansion for *LP* = 46 cm. Side view of plasma expansion in an ambient Ar gas, at 2 μs after the laser pulse for various focusing conditions (d), and at various delays for *LP* = 46 cm (e).

The particular V-shape plasma emission was recorded only for the side-view, while the top-view images (Fig. 2c) display a more classical elongated plasma shape. One can therefore speculate on a possible correlation between this different behavior in the two perpendicular planes and the different energy distribution on the long and short axes of the laser beam. Moreover, the different dimensions of the beam on the two axes (see Figures 1b,c) can generate the flip-over effect [38], which seems to be verified here.

To get more insight into the dynamics of this particular V-shape of plasma, the effect of an ambient Ar gas was additionally investigated (Fig. 2d). The usual decelerating effect and radiation emission enhancement as consequence of the kinetic energy conversion [39] can be noticed for all investigated focusing conditions. The existence of a central plasma structure made of fast ejected particles in the case of V-like plasma shape (*LP*=46 cm) becomes more obvious than for the in vacuum expansion. Preserving a relatively high pressure of 5 Pa and varying the time delays after the laser pulse, the dynamics of the fast-central plasma structure becomes clearer (see dotted marks in Fig. 2e). According with [19,40], there are in general two main mechanisms responsible for the increased emission of radiation: i) excitations through collisions with the ambient gas, ii) and (dominantly) the electron impact processes, which through secondary ionizations enhance electron density and thus excitations of atomic and ionic species [40]. In this context, the influence of the background gas ionization potential and atomic mass are well-known in the literature [41,42].

As regarding the vacuum plasma expansion, the emission intensities along the *Z*-axis (Fig. 3a) at various delays were extracted by cross-sectioning each side-view image (time sequences of Fig. 2b), to contour plot as a function of both time and distance from the target – Fig. 3b. A linear dependence of the maximum emission spot (taken from Fig. 3a and which correspond to the crossing point of the V arms) on the delay was evidenced. One can thus derive an expansion velocity v_{cross}=3.3·10^3 m/s. We mention that under vacuum conditions, the fast central plasma structure mentioned above is not emissive enough to allow an estimation of its velocity.

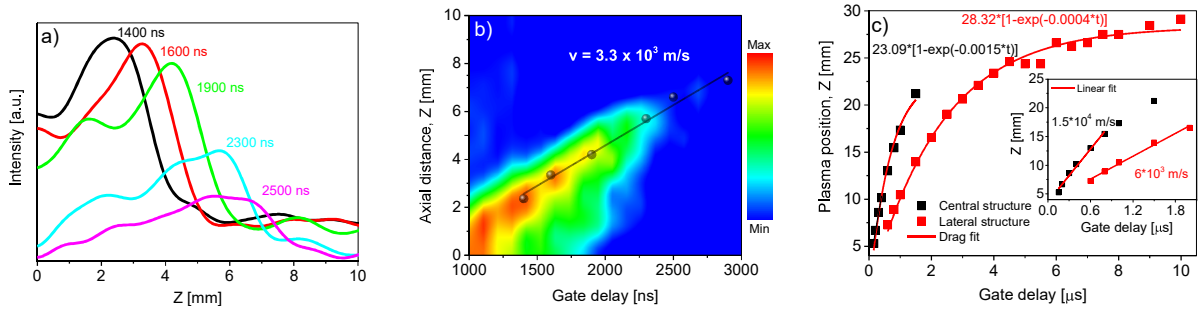

Fig. 3. Carbon excimer LPP expansion: in vacuum – a) derived ICCD *Z*-axis intensity profiles at different delays after the laser pulse, b) space-time contour plot of emission intensity along *Z*-axis and the obtained expansion velocity of the slow structure, and c) in Ar background gas – time-dependence of maximum emissivity position with corresponding initial velocities (inset) of central and lateral structures.

The rapidly expanding structure can be clearly observed when plasma evolution takes place in ambient Ar gas. By similar cross-sectioning ICCD images and plotting the maximum emissivity positions of the fast central structure (dotted in Fig. 2e) *vs*. delay – Fig. 3c, we obtain an initial linear dependence for gate delay below 1 μs (see the inset of Fig. 3c). The corresponding velocity is v_{fast}=1.5·10^4 m/s, that is one order of magnitude higher when compared with the V-shape plasma structure expansion velocity in vacuum. After the initial stages, the fast ejected particles are slowed down, and the time-dependence of maximum emissivity positions obeys the well-known drag model [43–45], as the fittings from Fig. 3c show. The lateral arms of the V-shape, which were transformed by the background gas in two radiating balls (see Fig. 2e), reveal a similar behavior of each ball maximum intensity position *vs.* time: at early expansion times (below 2μs – see the inset of Fig. 3c), the dependence is linear and the resulting initial expansion velocity along *Z*-axis is found to be v_z=6·10^3 m/s. Then, the flight of the lateral structures was found to become almost parallel with a distance of about 10 mm between them, and their *Z*-position is again in good agreement with the drag model.

A possible correlation between the expanding plasma shape and the resulted crater depth profile is further investigated. In Fig. 4 we display the crater three-dimensional geometry obtained after 50 laser

pulses, for *LP* varying between 41 cm and 46 cm, where the expected increase of ablated volume and depth with laser fluence can be observed. The laser beam Gaussian short-axis energy distribution is generally mirrored in the crater depth profile along the *Y*-axis. This seems to be different for the long-axis. The top-hat profile is preserved only for low fluences, *e.g.* for *LP*=41 cm, while a two-step shape with a deeper hole in the centre was measured along the *X*-axis for *LP*=46 cm. Such unusual crater profile was previously reported in the literature [46], but for different experimental conditions: Q-switched Nd:YAG laser operating at 1064 nm in 10 ns pulses, ablating Al target in atmospheric environment, for fluences between 90 J/cm^2 and 300 J/cm^2. The authors studied ablated volume and crater shape in a wider range of fluences, between 1.5 and 840 J/cm^2, suggesting the existence of four laser fluence ranges through the crater types, the results being correlated with the trend of integrated spectral line intensities of Al II (281.6 nm) and Al I (305.0 nm). Moreover, our preliminary results using other types of targets (to be detailed in a future publication) showed that the unusual V-shape emission is particular for the carbon plasma plume.

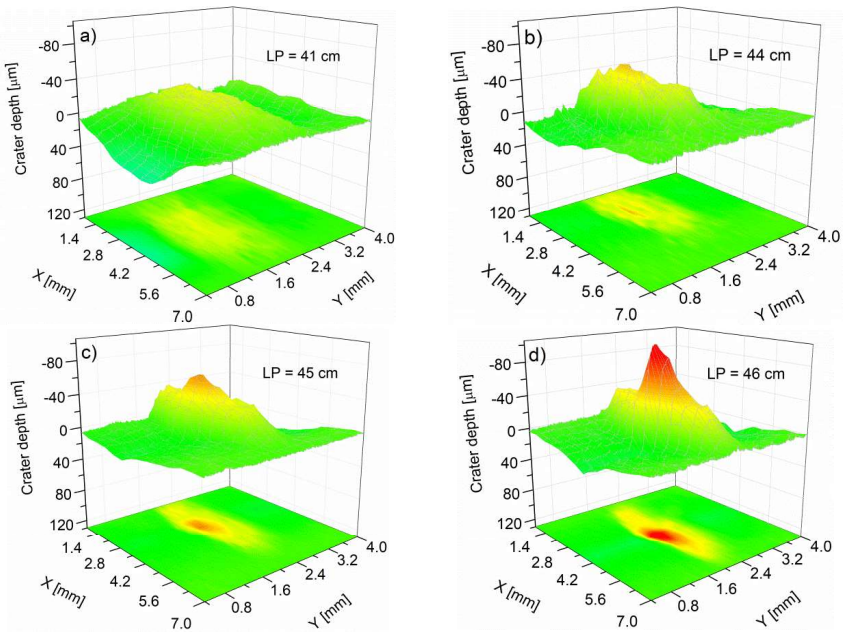

Fig. 4. Laser ablation crater depth profiles as a function of the beam focusing.

Now returning to the initial discussion on the energy distribution of the laser spot, the far field energy profile is narrower than the near-field one, as can be observed form Fig. 1b and Fig. 1c. Considering the high M^2 factor characteristic to excimer lasers, it is expected that, after focusing, the profiles become smoother for the short-axis compared to the long one. On the other hand, the focusing at the ablation spot is tighter along the short axis, which also explains the shape of the crater presented in Fig. 4. Therefore, we can simplify the discussion by proposing a scenario based on the interaction of three different plasmas having the origins along the *X*-axis of the beam: the central area of the laser spot with a higher energy density would give birth to the fast and hot axial plasma, while two lower energy density lateral spots would generate two colder side plasma structures (see Fig. 5). The interaction of these plasmas leads to the formation of different regions, as follows: regions 1 and 1' are free expansion areas of the two lateral plasmas; regions 2 and 2' are interaction zones at the borders between the central plasma and the two lateral plasmas; and, finally, region 3 represents the interaction zone of central plasma and particles coming from lateral sides. The interaction of the three plasmas in the areas denoted by 2-2' in Fig. 5, leads to the sliding of the lateral plasmas on the higher density central plasma. Also, the greater expansion velocity of plasma region 3 leaves behind the regions 2 and 2', which are just the two arms of the V-shape plasma highlighted by the ICCD images.

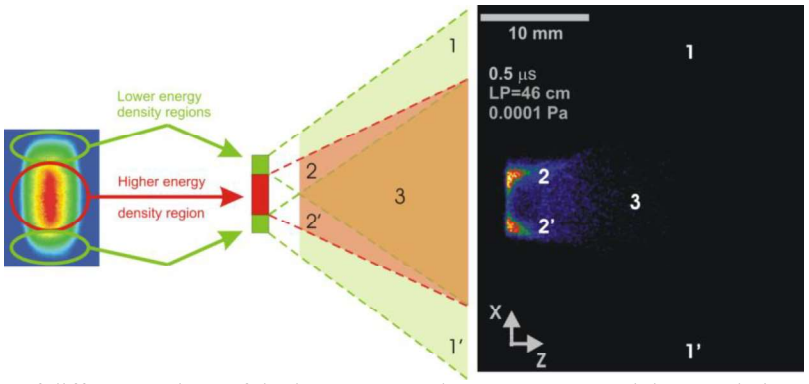

Fig. 5. Assignment of different regions of the laser spot as plasmas sources and the correlations with the V-shape plasma structure.

3.2. Space-resolved optical spectra and individual species expansion velocities

In order to better understand the plasma evolution process, the atomic and ionic species were monitored using OES, by recording the spectra of ~1 mm^2 emitting regions of plasma along the *X* and *Z* directions. We first considered only the spectral data recorded for a delay to the laser pulse greater than 150 ns, in order to obtain a low level of continuum given by Bremsstrahlung radiation and free–bound electronic transitions.

In Fig. 6a, the typical wide spectra recorded are presented for various *X*-distances from the plasma symmetry plane (*OYZ*), at *Z*=2.5 mm from the target surface and tight focusing of the laser beam (*LP*=46 mm). A recording gate width of 5 µs was used to ensure significant visible emission signals for all plasma species in the considered experimental conditions. The assigned spectral features show the presence of C_2 molecules through the Swan bands corresponding to various differences of the vibrational quantum number ($\Delta v = -1,0,1,2$). Also, several emission lines can be clearly identified as corresponding to CI (λ=437.13 nm, λ=477.16 nm, λ=493.21 nm, λ=538.03 nm and λ=833.5 nm) and CII (λ=426.72 nm, λ=504.07 nm and λ=566.24 nm) species [47]. Lines intensity dependence with *X*-coordinate is in agreement with previous sequential side-view images: a maximum of emission is recorded for *X*=5 mm for all species, *i.e.* for the lateral arms seeds of V-shape plasma, while in the center (*X*=0) a minimum is observed.

For time-resolved OES measurements, the gate width was decreased to 50 ns and for a good signal-to-noise ratio, accumulations of signals from 100 laser pulses were used. The most intense lines of each species were then selected, *i.e.* C_2: 516.64 nm (*v*-*v'*=0-0), CI: 505.21 nm and CII: 504.07 nm, in a narrow wavelength range. The dependence of specified lines intensities *vs*. *X*-position (Fig. 6b) reveals a maximum at 5 mm, when the observation point descends along the *X*-axis in the first slice of plasma (*Z*=0) parallel with the target surface. The dominance of C_2 molecules over neutral and singly-ionized atoms in the plasma lateral arms observed by ICCD fast imaging can be a first argument for a recombination process, recently reported in the literature [15], which is thought to be at the origin of the carbon dimer formation.

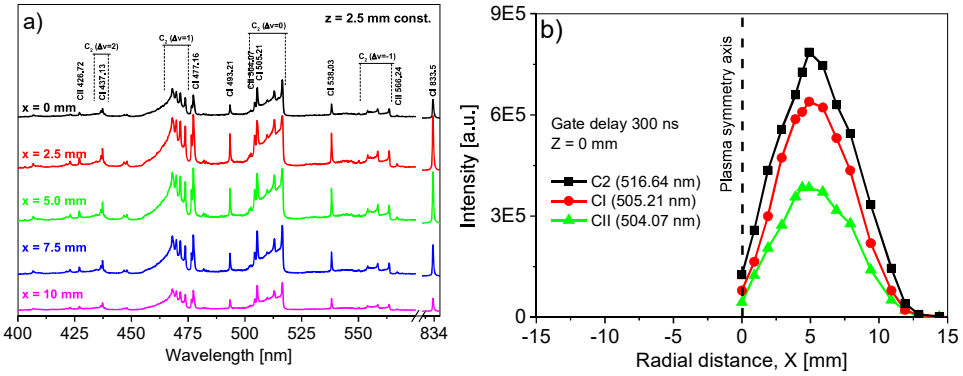

Fig. 6. Lateral (*X*-axis) variation of the emission spectra (*LP*=46 mm, gate width 5 μs, gate delay 150 ns) at *Z*=2.5 mm away from the target surface (a) and lateral profiles of the plasma species emission recorded very close to the target surface (*Z*=0 mm) for 300 ns gate delay (b).

Time of flight (TOF) signals of different plasma species, recorded along the expansion direction normal to the target at various distances, are presented in Figs. 7a-7d (solid line is used just for guiding the eye). One can observe that each species has its own time of maximum emission intensity when compared for similar recording distances, and moreover it depends on the chosen electronic transition. Then, extracting the dependence between the *Z*-distance from the target and the time corresponding to maximum intensity of selected spectral lines (see the insets of Figs. 7a-7d), a linear behavior was obtained, which allows calculation of expansion velocities. The resulted values have the same order of magnitude as the values corresponding to the fast plasma structure deduced from ICCD imaging, although the emission process is more complex, involving more parameters (particle densities, collisional excitation rates, radiative de-excitation rates, etc.), which can affect the physical significance of the derived expansion velocity. However, we should note the high value of C_2 velocity, *i.e.* the shortest time of emission for C_2 molecule, when compared with CI or CII that are emitting over a longer time range. Also, the most significant emission of C_2 is near the target surface, while CI and CII are observed up to tens of millimeters away. These allow us to conclude that for the fast-central part of the plasma most of the C_2 molecules are the result of three-body recombination processes.

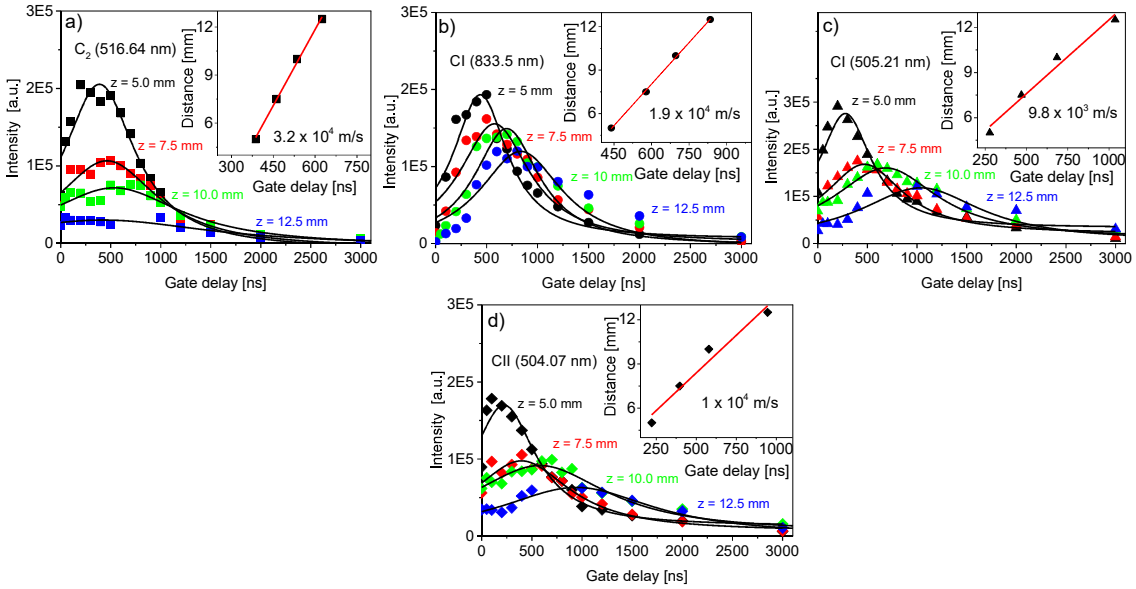

Fig. 7. Time of flight (TOF) emission profiles of various plasma species at various distances from the target (a)-(d), for tight focusing of the laser beam (*LP*=46 cm) and maximum emission positions *vs.* time-delays of each species with derived expansion velocities presented as insets.

3.3. Angular distribution of TOF ion signal recorded by FC.

To have a more comprehensive description of the plasma species, we further use the electrical characterization by means of a Faraday cup. The collector was initially placed at 14 cm from the target surface in normal direction and TOF ion signals were recorded in various focusing conditions (Fig. 8a).

An expected increase of the total collected charge with the laser fluence can be observed, while the signal shape fits well the time-dependence deduced from a shifted-Maxwell-Boltzmann (SMB) distribution function [20,48]. The existence of fast and slow plasma structures is not clearly evidenced by two distinct current peaks, but a small hump in the descendant region (see the arrow mark in Fig. 8a) can be distinguished, and it corresponds to the cold structure detaching from the target at later times. Having in view also the previous results from ICCD imaging and OES, we consider the dominant contribution of the fast part to the FC signal. In these circumstances, we are able to deduce several global plasma parameters corresponding to the fast structure, by means of the function:

$$I(t) \propto A\, t^{-3} \exp\left[-\frac{m_i}{2k_B T}(d/t - v_D)^2\right] = A\, t^{-3} \exp\left[-\left(\frac{d/t - v_D}{v_{T\square}}\right)^2\right] \quad (1)$$

with A a constant imposed by the ion density and the FC entrance area, m_i the ion mass, T the plasma temperature, d the target-FC distance, v_D the expanding plasma drift velocity and v_{Th} the thermal velocity.

The results plotted in Fig. 8b show an initial increase of the plasma temperature *vs*. laser fluence, followed by a saturation trend at about 13 eV, while the behavior of the drift velocity is opposite, being almost constant, v_D=1.2·10^4 m/s at low fluences and increasing to v_D=1.4·10^4 m/s for *LP*=46 mm. This value is in good agreement with the ones deduced through optical methods for the fast central structure.

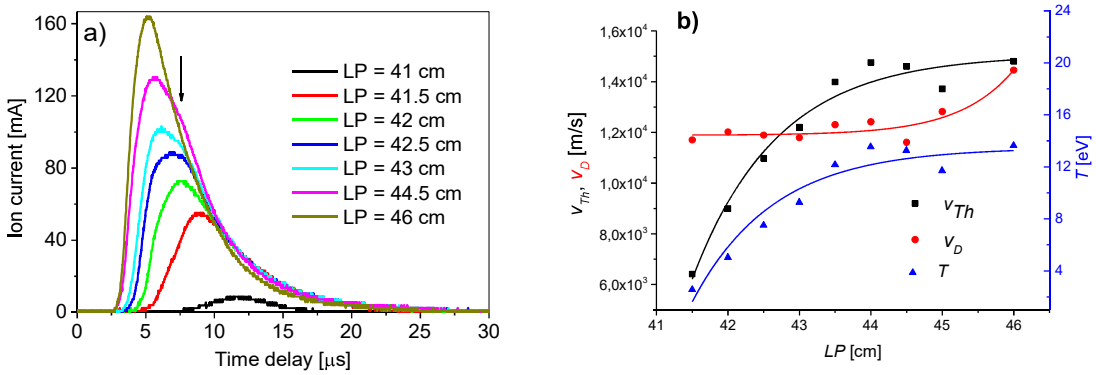

Fig. 8. TOF ion signals recorded by FC placed on normal direction to the target at a distance of *z*=14 cm for various laser fluences (a) and derived plasma global parameters (b).

Let us further study the angular distribution of the ejected ions. Preserving the distance of 14 cm form the target surface, TOF ion signals were recorded for *LP*=46 cm at various angles with respect to the *z*-axis, rotating the FC around the long and the short laser beam axes (see Fig. 1a). The recorded temporal traces were used to build contour plot representations, which are presented in Figs. 9a-c for different focusing conditions. We observed the most significant ion ejection on normal direction (θ=0^0) regardless of the *LP*, while the number of ions is increasing with the laser fluence for all angular directions. The first observation for *LP*=46 cm is surprising, since in Fig. 2b most of the visible radiation comes from the lateral arms of the V-shape, but considering the highest depth in the crater central part (Figure 4d) it becomes explainable. Moreover, changing the angle by moving away from the plasma *z*-axis, we observe a shift of the maximum current position to higher time values (Fig. 9c), which corresponds to a contribution of the signal from the positive charged particles coming from the slow arms of the plasma. Consequently, we conclude that the initial central plasma part consists in highly charged, fast and hot, but

low radiation emitting particles, followed by a mostly neutral slow part, radiating mainly in the lateral sides.

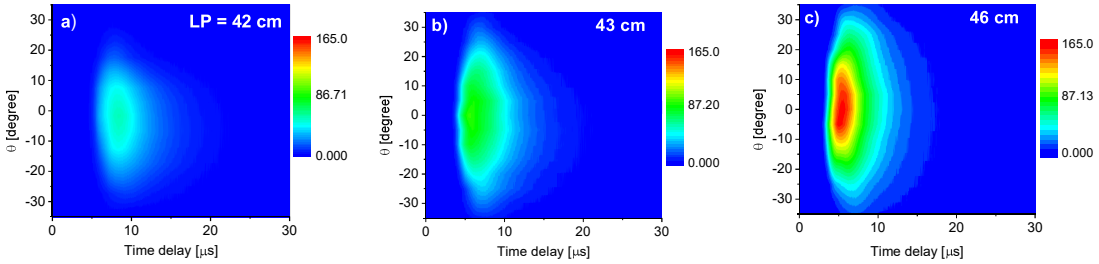

Fig. 9. Contour plots of angular dependences of ion current temporal traces at 14cm from the center of laser beam impact point for *LP*=42 cm (a), *LP*=43 cm (b), and *LP*=46 cm (c).

The angular distribution of the ion current is usually described by the Anisimov model [33,38,49], which fits well also our experimental data, through the dependence:

$$i_{max}(\theta) = A(1+\tan^2\theta)^{3/2}(1+k^2\tan^2\theta)^{-3/2} \quad (2)$$

of maximum current values, for θ up to ≈60°, where A is the peak intensity value at $\theta = 0$ and k is the asymptotic value of the longitudinal-to-transverse ratio of the plume in the plane of observation. In Fig. 10a, such fits are presented for *LP*=46 cm, *LP*=43 cm and *LP*=42 cm, along with the resulted values of A and k constants, where the determination coefficient was obtained higher than 99.5%. Moreover, for the short axis of the laser beam, the angular dependence obeys the same law, as plotted in Fig. 10b for *LP*=46 cm. We note that angular dependence of the ion current on the laser short axis was monitored up to -30^0 (the red symbols from Fig. 10b) in order to avoid blocking the ablation laser beam by the FC.

Returning to the dependence given by Eq. (1) resulted from SMB distribution function, numerical fittings of the FC ion temporal traces allow calculation of ion temperature and drift velocity angular distributions, the results being presented in Fig. 10c for *LP*=46 cm and *LP*=42 cm. We observe a significant decrease for *LP*=46 cm from about 13 eV on normal direction, to less than 4 eV at $\pm 40^0$, while the drift velocity (not shown) resulted to be almost constant, of about $1.45 \cdot 10^4$ m/s, with low variations in the limits of determination errors.

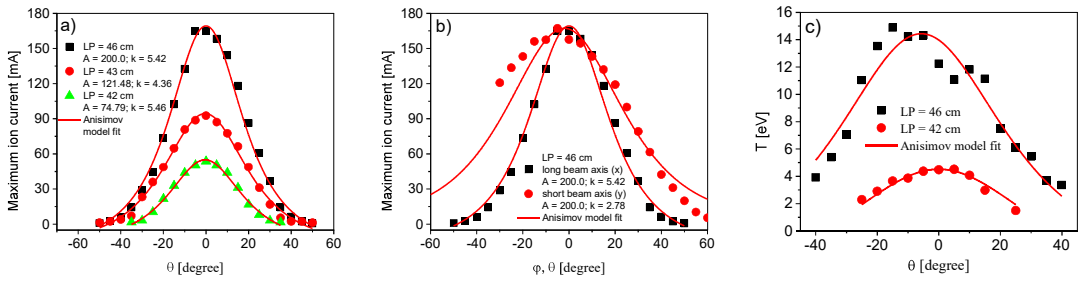

Fig. 10. Maximum ion current angular dependence for various *LP*s (a), comparison between long- and short-axis dependence for *LP*=46 cm (b), and ion temperature angular distribution for *LP*=46 cm and *LP*=42 cm (c).

In order to have an overview on this particular V-like case of carbon excimer laser-produced plasma, we plot in Fig. 11 the radial dependence of the radiation intensity emitted by various plasma species, along with the angular variation of the maximum ion current. We note that some instrumental limitations allowed spectral measurements only for positive radial X-distances, but in the assumption of plasma shape Z-axis symmetry (clearly seen from ICCD images), they can be mirrored also in the negative range.

Finally, the scenario of three plasmas interaction proposed above becomes more obvious. The three collinear focalization spots represented in Fig. 5 stay at the origin of three plasmas simultaneous

formation. The central spot, where the incident laser beam has the highest energy density, gives rise to a fast expanding plasma of a high ionization degree (giving the maximum of ion signal) that expand also in lateral direction, toward two another plasmas constituted in lateral sides, from the lower energy density areas of the incident laser beam. The interaction between these neighboring plasmas leads to the formation of two symmetrical arms characterized by an increased number of collisions, *i.e.* by an enhanced emission of radiation. On the other hand, the maximum of the ion flux recorded for the low emissivity central area of plasma can be explained by the high expansion velocity of this region, and by the increased number of ions.

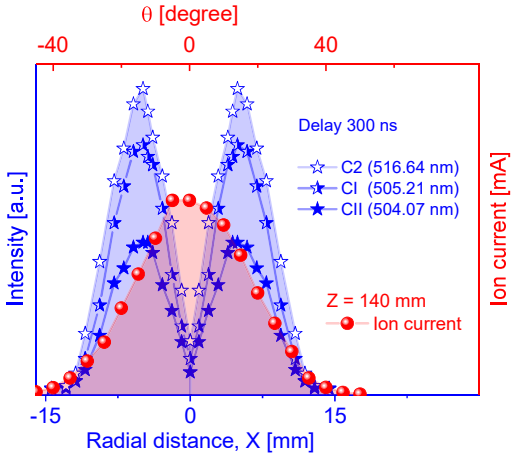

Fig. 11. Radial and angular distribution of optically and electrically investigated plasma species.

4. Conclusions

A particular V-shape laser-produced carbon plasma generated by excimer laser ablation of graphite in vacuum was investigated by various techniques and its formation was explained by the interaction of three neighboring ablation plasmas, originating in three different energy density regions delimited on the same laser focalization spot: a central one, where the incident laser beam has a high energy density, that gives rise to a fast expanding plasma, and two other lower energy density lateral areas, that lead to the formation of slower expanding plasmas. The ejection of the fast central plasma and the interaction with the slower lateral plasmas determine such particular V-shape carbon ablation plasma. Moreover, the colliding of plasmas leads to an enhancement of carbon dimer formation in an area that is more significant than the usually reported on carbon laser-produced plasma expansion in vacuum (near the target roughly up to 12.5 mm in all directions).

Crater profile investigations evidenced a deeper central region for high laser fluence, which is connected with the unusual V-shape through different ablation regimes. The dominance of the spectral features of C_2 molecules in the optical emission spectra recorded for the lateral regions (*i.e.* interaction regions), mainly radiating near the target surface and having the shortest time decay, allowed concluding that these species are the result of a three-body recombination process. Moreover, the electrical measurements using a Faraday cup placed at various angular positions with respect to the target normal strengthens this hypothesis. The angular dependence of the ion saturation signal shows a maximum on the axial expansion direction while moving toward the lateral regions the interaction processes increase and ion saturation signal decays continuously. The observed enrichment in carbon dimers in the V-shape laser-produced plasma is considered to be favorable for the deposition of high quality carbon-based nanostructures, which will be the subject of our further investigations.

Acknowledgements

Part of this work was supported by the Romanian Space Agency (ROSA) within Space Technology and Advanced Research (STAR) Program (Project no.: 169/20.07.2017).

References

[1] A.A. Puretzky, D.B. Geohegan, X. Fan, S.J. Pennycook, Dynamics of single-wall carbon nanotube synthesis by laser vaporization, Appl. Phys. A Mater. Sci. Process. 70 (2000) 153–160.

[2] S.S. Harilal, R.C. Issac, C. V Bindhu, V.P.N. Nampoori, C.P.G. Vallabhan, Optical emission studies of C_2 species in laser-produced plasma from carbon, J. Phys. D. Appl. Phys. 30 (1997) 1703–1709.

[3] D.H. Lowndes, D.B. Geohegan, A.A. Puretzky, D.P. Norton, C.M. Rouleau, Synthesis of novel thin-film materials by pulsed laser deposition, Science 273 (1996) 898–903.

[4] L. Torrisi, F. Caridi, D. Margarone, A. Picciotto, A. Mangione, J.J. Beltrano, Carbon-plasma produced in vacuum by 532 nm-3 ns laser pulses ablation, Appl. Surf. Sci. 252 (2006) 6383–6389.

[5] H.M. Ruiz, F. Guzmán, M. Favre, H. Bhuyan, H. Chuaqui, E.S. Wyndham, Time- and space-resolved spectroscopic characterization of a laser carbon plasma plume in an argon background, Plasma Sources Sci. Technol. 21 (2012) 034014.

[6] F. Guzmán, M. Favre, H.M. Ruiz, S. Hevia, L.S. Caballero, E.S. Wyndham, H. Bhuyan, M. Flores, S. Mändl, Pulsed laser deposition of thin carbon films in a neutral gas background, J. Phys. D. Appl. Phys. 46 (2013) 215202.

[7] K.F. Al-Shboul, S.S. Harilal, A. Hassanein, M. Polek, Dynamics of C_2 formation in laser-produced carbon plasma in helium environment, J. Appl. Phys. 109 (2011) 053302.

[8] E.A. Rohlfing, D.M. Cox, A. Kaldor, Production and characterization of supersonic carbon cluster beams, J. Chem. Phys. 81 (1984) 3322–3330.

[9] C. Lifshitz, Carbon clusters, Int. J. Mass Spectrom. 200 (2000) 423–442.

[10] K. Sasaki, T. Wakasaki, S. Matsui, K. Kadota, Distributions of C_2 and C_3 radical densities in laser-ablation carbon plumes measured by laser-induced fluorescence imaging spectroscopy, J. Appl. Phys. 91 (2002) 4033–4039.

[11] K.F. Al-Shboul, S.S. Harilal, A. Hassanein, Emission features of femtosecond laser ablated carbon plasma in ambient helium, J. Appl. Phys. 113 (2013) 163305.

[12] K.F. Al-Shboul, S.S. Harilal, S.M. Hassan, A. Hassanein, J.T. Costello, T. Yabuuchi, K.A. Tanaka, Y. Hirooka, Interpenetration and stagnation in colliding laser plasmas, Phys. Plasmas. 21 (2014) 013502.

[13] N. Gambino, P. Hayden, D. Mascali, J. Costello, C. Fallon, P. Hough, P. Yeates, A. Anzalone, F. Musumeci, S. Tudisco, Dynamics of colliding aluminium plasmas produced by laser ablation, Appl. Surf. Sci. 272 (2013) 69–75.

[14] T. Sizyuk, J. Oliver, P.K. Diwakar, Mechanisms of carbon dimer formation in colliding laser-produced carbon plasmas, J. Appl. Phys. 122 (2017) 023303.

[15] K.F. Al-Shboul, S.M. Hassan, S.S. Harilal, Molecular formation in the stagnation region of colliding laser-produced plasmas, Plasma Sources Sci. Technol. 25 (2016) 65017.

[16] V.S.S. Burakov, A.F.F. Bokhonov, M.I.I. Nedel'ko, N.A.A. Savastenko, N.V. V. Tarasenko, Dynamics of the emission of light by C_2 and C_3 molecules in a laser plasma produced by two-pulse irradiation of the target, J. Appl. Spectrosc. 69 (2002) 907–912.

[17] M. Favre, H.M. Ruiz, L.S.C. Bendixsen, S. Reyes, F. Veloso, E. Wyndham, H. Bhuyan, Effects of a static inhomogeneous magnetic field acting on a laser-produced carbon plasma plume, AIP Adv. 7 (2017) 085002.

[18] A. Neogi, R.K. Thareja, Dynamics of laser produced carbon plasma expanding in a nonuniform magnetic field, J. Appl. Phys. 85 (1999) 1131–1136.

[19] A. Kushwaha, R.K. Thareja, Dynamics of laser-ablated carbon plasma: formation of C_2 and CN., Appl. Opt. 47 (2008) G65-G71.

[20] P. Nica, S. Gurlui, M. Osiac, M. Agop, M. Ziskind, C. Focsa, Investigation of femtosecond laser-produced plasma from various metallic targets using the Langmuir probe characteristic, Phys. Plasmas. 24 (2017) 103119.

[21] P. Nica, M. Agop, S. Gurlui, C. Focsa, Oscillatory Langmuir probe ion current in laser-produced plasma expansion, EPL (Europhysics Lett. 89 (2010) 65001.

[22] C. Focsa, S. Gurlui, P. Nica, M. Agop, M. Ziskind, Plume splitting and oscillatory behavior in transient plasmas generated by high-fluence laser ablation in vacuum, Appl. Surf. Sci. 424 (2017) 299–309.
[23] O. Balki, H.E. Elsayed-Ali, Multicharged carbon ion generation from laser plasma, Rev. Sci. Instrum. 87 (2016) 113304.
[24] P.-E. Nica, G.B. Rusu, O.-G. Dragos, C. Ursu, Effect of Excimer Laser Beam Spot Size on Carbon Laser-Produced Plasma Dynamics, IEEE Trans. Plasma Sci. 42 (2014) 2694–2695.
[25] C. Ursu, P. Nica, Diagnosis of carbon laser produced plasma by using an electrostatic energy analyzer, J. Optoelectron. Adv. Mater. 15 (2013) 42–45.
[26] C. Focsa, J.L. Destombes, $Na/K(H_2O)_n$ clusters produced by laser desorption of Na/K salt doped ice, Chem. Phys. Lett. 347 (2001) 390–396.
[27] R. Kelly, R.W. Dreyfus, On the effect of Knudsen-layer formation on studies of vaporization, sputtering, and desorption, Surf. Sci. 198 (1988) 263–276.
[28] C. Mihesan, N. Lebrun, M. Ziskind, B. Chazallon, C. Focsa, J.L. Destombes, IR laser resonant desorption of formaldehyde–H_2O ices: hydrated cluster formation and velocity distribution, Surf. Sci. 566–568 (2004) 650–658.
[29] C. Focsa, B. Chazallon, J.L. Destombes, Resonant desorption of ice with a tunable $LiNbO_3$ optical parametric oscillator, Surf. Sci. 528 (2003) 189–195.
[30] M.R. Perrone, S. Tundo, C. Panzera, G. De Nunzio, Beam-divergence control of excimers with plane-parallel Gaussian cavities, Appl. Opt. 36 (1997) 8574.
[31] R.F. Wood, K.R. Chen, J.N. Leboeuf, A.A. Puretzky, D.B. Geohegan, Dynamics of plume propagation and splitting during pulsed-laser ablation, Phys. Rev. Lett. 79 (1997) 1571–1574.
[32] C. Focsa, P. Nemec, M. Ziskind, C. Ursu, S. Gurlui, V. Nazabal, Laser ablation of As_xSe_{100-x} chalcogenide glasses: Plume investigations, Appl. Surf. Sci. 255 (2009) 5307–5311.
[33] K.K. Anoop, X. Ni, X. Wang, S. Amoruso, R. Bruzzese, Fast ion generation in femtosecond laser ablation of a metallic target at moderate laser intensity, Laser Phys. 24 (2014) 105902.
[34] K.K. Anoop, S.S. Harilal, R. Philip, R. Bruzzese, S. Amoruso, Laser fluence dependence on emission dynamics of ultrafast laser induced copper plasma, J. Appl. Phys. 120 (2016) 185901.
[35] P.-E.P.-E.P. Nica, M. Agop, S. Gurlui, C. Bejinariu, C. Focsa, Characterization of aluminum laser produced plasma by target current measurements, Jpn. J. Appl. Phys. 51 (2012) 106102.
[36] N.M. Bulgakova, A. V. Bulgakov, O.F. Bobrenok, Double layer effects in laser-ablation plasma plumes, Phys. Rev. E. 62 (2000) 5624–5635.
[37] C. Ursu, O.G.G. Pompilian, S. Gurlui, P. Nica, M. Agop, M. Dudeck, C. Focsa, Al_2O_3 ceramics under high-fluence irradiation: plasma plume dynamics through space- and time-resolved optical emission spectroscopy, Appl. Phys. A Mater. Sci. Process. 101 (2010) 153–159.
[38] S.I. Anisimov, B.S. Luk'yanchuk, A. Luches, An analytical model for three-dimensional laser plume expansion into vacuum in hydrodynamic regime, Appl. Surf. Sci. 96–98 (1996) 24–32.
[39] J. Schou, S. Amoruso, J.G. Lunney, Plume Dynamics, in: Laser Ablation Its Appl., Springer US, Boston, MA, 2006: pp. 67–95.
[40] A. Kumar, R.K. Singh, K.P. Subramanian, B.G. Patel, S. Sunil, I.A. Prajapati, Effects of ambient pressure and laser fluence on the temporal evolution of 426.7 nm CII line in laser-blow-off of multilayered LiF-C thin film, J. Phys. D. Appl. Phys. 39 (2006) 4860–4866.
[41] J. Gonzalo, C.N. Afonso, I. Madariaga, Expansion dynamics of the plasma produced by laser ablation of BaTiO3 in a gas environment, J. Appl. Phys. 81 (1997) 951–955.
[42] S. Amoruso, J. Schou, J.G. Lunney, Influence of the atomic mass of the background gas on laser ablation plume propagation, Appl. Phys. A. 92 (2008) 907–911.
[43] D.B. Geohegan, Fast intensified- CCD photography of $YBa_2Cu_3O_{7-x}$ laser ablation in vacuum and ambient oxygen, Appl. Phys. Lett. 60 (1992) 2732–2734.
[44] A.K. Sharma, R.K. Thareja, Characterization of laser-produced aluminum plasma in ambient atmosphere of nitrogen using fast photography, Appl. Phys. Lett. 84 (2004) 4490–4492.
[45] S.S. Harilal, C. V. Bindhu, M.S. Tillack, F. Najmabadi, A.C. Gaeris, Internal structure and expansion

dynamics of laser ablation plumes into ambient gases, J. Appl. Phys. 93 (2003) 2380–2388.
[46] G. Cristoforetti, S. Legnaioli, V. Palleschi, E. Tognoni, P.A. Benedetti, Observation of different mass removal regimes during the laser ablation of an aluminium target in air, J. Anal. At. Spectrom. 23 (2008) 1518.
[47] https://www.nist.gov/pml/atomic-spectra-database, (n.d.).
[48] J.C.S. Kools, T.S. Baller, S.T. De Zwart, J. Dieleman, Gas flow dynamics in laser ablation deposition, J. Appl. Phys. 71 (1992) 4547–4556.
[49] B. Toftmann, J. Schou, T. Hansen, J. Lunney, Angular distribution of electron temperature and density in a laser-ablation plume, Phys. Rev. Lett. 84 (2000) 3998–4001.